OPEN ACCESS

International
Journal
Of Modern Engineering Research (IJMER)

Energy Management of Distributed Generation Inverters using MPC Controller in a MICROGRID Applications

Mohana. P[1], Sivanagaraju. S. V[2]
[1,2] *Department of Electrical and Electronics Engineering, JNTU Anantapur*

Abstract: *This paper presents a microgrid consisting of different distributed generation (DG) units that are connected to the distribution grid. An energy-management algorithm is implemented to coordinate the operations of the different DG units in the microgrid for grid-connected and islanded operations. The proposed microgrid consists of a photovoltaic (PV) array which functions as the primary generation unit of the microgrid and a proton-exchange membrane fuel cell to supplement the variability in the power generated by the PV array. A lithium-ion storage battery is incorporated into the microgrid to mitigate peak demands during grid-connected operation and to compensate for any shortage in the generated power during islanded operation. The control design for the DG inverters employs a new model predictive control algorithm which enables faster computational time for large power systems by optimizing the steady-state and the transient control problems separately. The design concept is verified through various test scenarios to demonstrate the operational capability of the proposed microgrid, and the obtained results are discussed.*

Index Terms: *Distributed generation (DG), energy management, microgrid, model predictive control (MPC).*

I. Introduction

Over the last decade, efficient and reliable communication and control technologies, coupled with an increase in smarter electrical facilities, such as electric vehicles and smart meters, have resulted in an increasing number of consumers participating in demand response management (DRM) [1]–[5]. The current research is also focused on achieving a smarter grid through demand-side management (DSM), increasing energy reserves and improving the power quality of the distribution system, such as harmonic compensation for nonlinear loads [5]–[8]. These new trends enable higher levels of penetration of renewable generation, such as wind and solar power into the grid. The integration of renewable sources can supplement the generation from the distribution grid. However, these renewable sources are intermittent in their generation and might compromise the reliability and stability of the distribution network. As a result, energy-storage devices, such as batteries and ultra-capacitors, are required to compensate for the variability in the renewable sources. The incorporation of energy-storage devices is also critical for managing peak demands and variations in the load demand. In this paper, a microgrid consisting of a photovoltaic (PV) array, a proton-exchange membrane fuel cell (PEMFC), and a lithium-ion storage battery (SB) is proposed. The PEMFC is used as a backup generator unit to compensate for the power generated by the intermittent nature of the PV array. The SB is implemented for peak shaving during grid-connected operation, and to supply power for any shortage in generated power during islanded operation and to maintain the stability of the distribution network. An energy-management algorithm is designed for the microgrid to coordinate the sharing of power among different DG units. The proposed controller for the inverters of DG units is based on a newly developed model predictive control (MPC) algorithm, which optimizes the steady-state and the transient control problems separately. In this way, the computation time is greatly reduced. In what follows, this paper provides a comprehensive solution for the operation of a microgrid which will simultaneously dispatch real and reactive power during both grid-connected and islanded operations, compensate for harmonics in the load currents, and perform peak shaving and load shedding under different operating conditions.

II. System Description And Modeling

A. System Description

Fig. 1 shows the configuration of the microgrid proposed in this paper that is designed to operate either in the grid-connected or islanded mode. The main DG unit comprises a 40-kW PV array and a 15-kW PEMFC, which are connected in parallel to the dc side of the DG inverter 1 through dc/dc boost converters to regulate the

dc-link voltage of the DG inverter at the desired level by delivering the necessary power. The PV array is implemented as the primary generation unit and the PEMFC is used to back up the intermittent generation of the PV array. When there is ample sunlight, the PV array operates in the MPPT mode to deliver maximum dc power P_{pv} which is discussed in detail in [9] and [10], and the output voltage of the PV array is permitted to vary within an allowable

TAN *et al.*: COORDINATED CONTROL AND ENERGY MANAGEMENT OF DG INVERTERS IN A MICROGRID

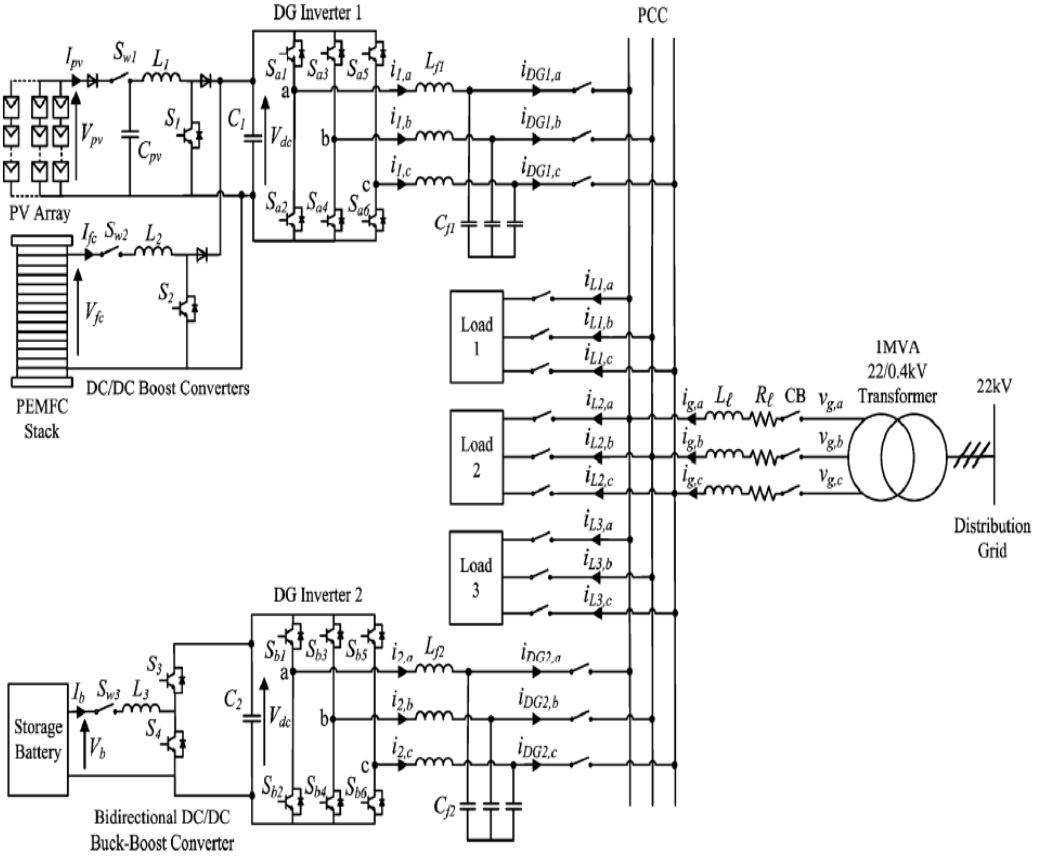

Fig. 1. Overall configuration of the proposed microgrid architecture.

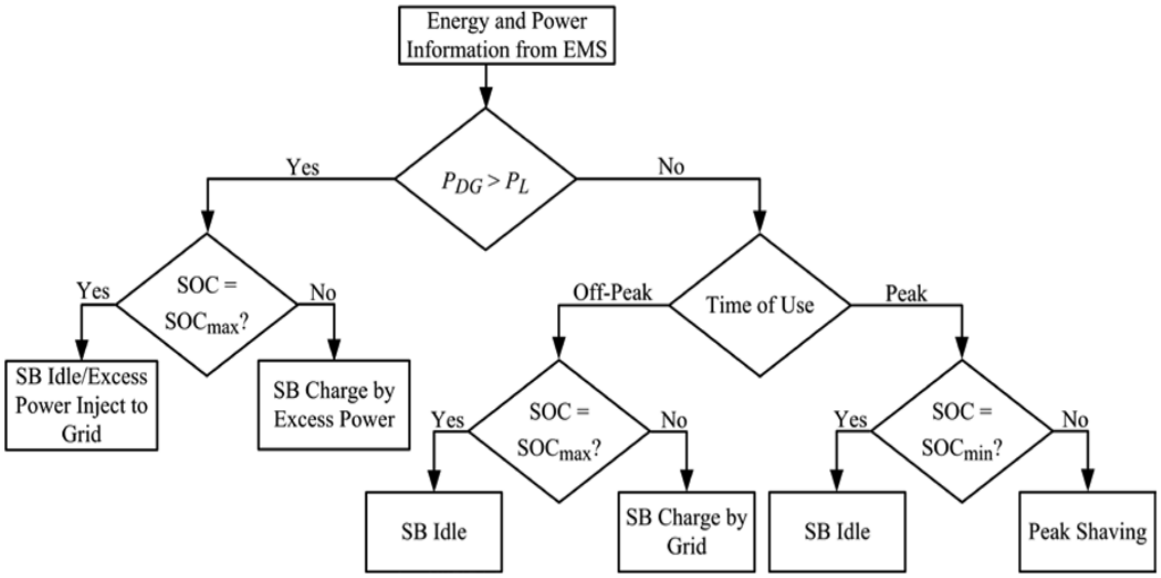

Fig. 2. Operation of the SB during grid-connected operation

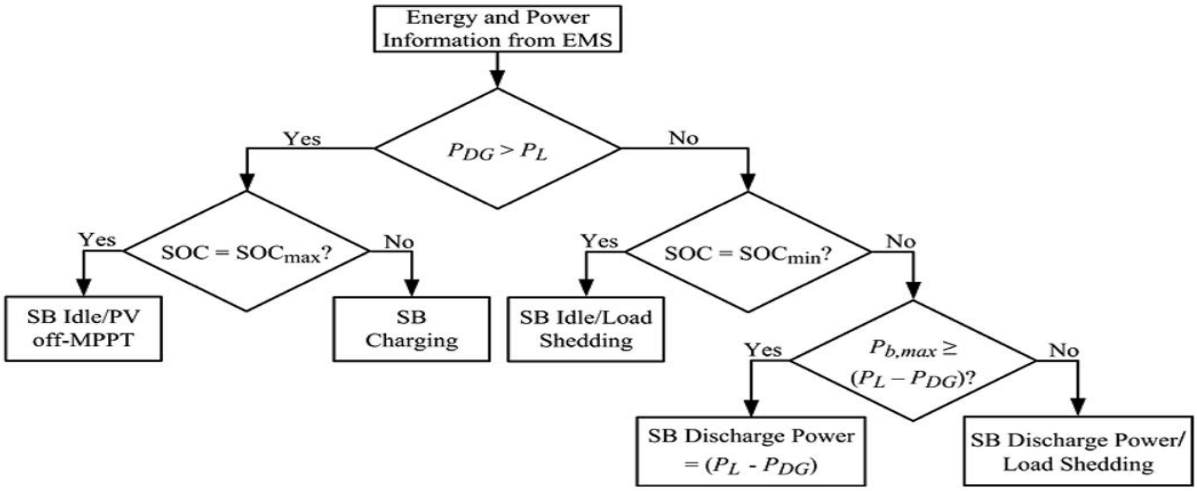

. Fig. 3. Operation of the SB during islanded operation

Range to ensure proper operation of the DG inverter. To maintain the level of the dc-link voltage at the required level, the PEMFC supplements the generation of the PV array to deliver the necessary $P_{fc.}$ when the output voltage of the PV array falls below a preset limit, the PV array is disconnected from the DG unit and the PEMFC functions as the main generation unit to deliver the required power. A 30-Ah lithium-ion SB is connected to the dc side of DG inverter2 through a bidirectional dc/dc buck-boost converter to facilitate the charging and discharging operations. During islanded operation, the role of the SB is to maintain the power balance in the microgrid which is given by

$$\boldsymbol{P_{DG}+P_b=P_L} \qquad \textbf{(1)}$$

Where P_{DG} is the power delivered by the main DG unit, P_b is the SB power which is subjected to the charging and discharging constraints given by

$$\boldsymbol{P_b \leq P_{b,max}} \qquad \textbf{(2)}$$

And P_L is the real power delivered to the loads. The energy constraints of the SB are determined based on the state-of-charge (SOC) limits which are given as

$$\boldsymbol{SOC_{min}} < SOC < \boldsymbol{SOC_{max}} \qquad \textbf{(3)}$$

Although the SOC of the battery cannot be measured directly, it can be determined through several estimation methods presented in [11] and [12]. When the microgrid operates islanded from the distribution grid, the SB can operate in the charging, discharging, or idle mode depending on its SOC and P_b . The flowcharts in Figs. 2 and 3 summarize the operation of the SB based on the output information provided by an energy-management system (EMS) during grid-connected and islanded operation, respectively. The EMS controls and monitors different aspects of power management, such as load forecasting, unit commitment, economic dispatch, and optimal power flow through a centralized server. Important information, such as field measurements from smart meters, transformer tap positions, and circuit- breaker (CB) status are all sent to the centralized server for processing through Ethernet. During grid-connected operation, the distribution grid is connected to the microgrid at the point of common coupling (PCC) through a circuit breaker (CB). The role of the main DG unit functions to provide local power and voltage support for the loads and, hence, reduces the burden of generation and delivery of power directly from the distribution grid. With the proliferation of power-electronics equipment being connected to the microgrid, the load currents could be distorted due to the presence of harmonic components. The DG units also function to compensate for any harmonics in the currents drawn by nonlinear loads in the microgrid, so that the harmonics will not propagate to other electrical networks connected to the PCC. Generally, there are variations in the power generated by the PV array and that demanded by the loads. If the power generated by the main DG unit is greater than the total load demand in the microgrid, the excess power can be used to charge the SB or injected into the distribution grid, depending on the SOC of the SB, as shown in Fig. 2. Conversely, when the total load demand is greater than the power generated by the main DG unit, the SB can be controlled to achieve different energy-management functions depending on its SOC and the time of use (TOU) of electricity. During off-peak periods as shown in Fig. 2, when the cost of generation from the grid is low and if the SB's SOC is below the maximum SOC limit , the SB can be charged by the grid and the loads will be supplied by the main DG unit and the grid. During peak periods, when the cost of generation from the grid is high and if the SB's SOC is above the minimum SOC limit , the SB can deliver

power to the grid to achieve peak shaving. When a fault occurs on the upstream network of the distribution grid, the CB operates to disconnect the microgrid from the distribution grid. The main DG unit and the SB are the sole power sources left to regulate the loads. In the case when the generation capacity of the main DG unit is unable to meet the total load demand, the SB is required to provide for the shortage in real and reactive power to maintain the power balance and stability of the microgrid as shown in Fig. 3. When the total load demand exceeds the generation capacity of the main DG unit and the SB, the EMS detects a drop in the system frequency and load shedding for noncritical loads is required to restore the system frequency and maintain the stability of the microgrid.

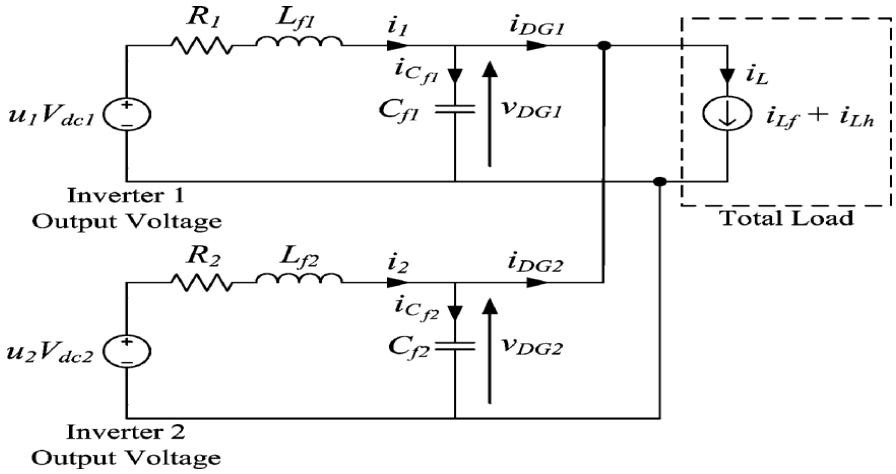

Fig. 4. Equivalent single-phase representation of the DG inverters for Grid connected operation

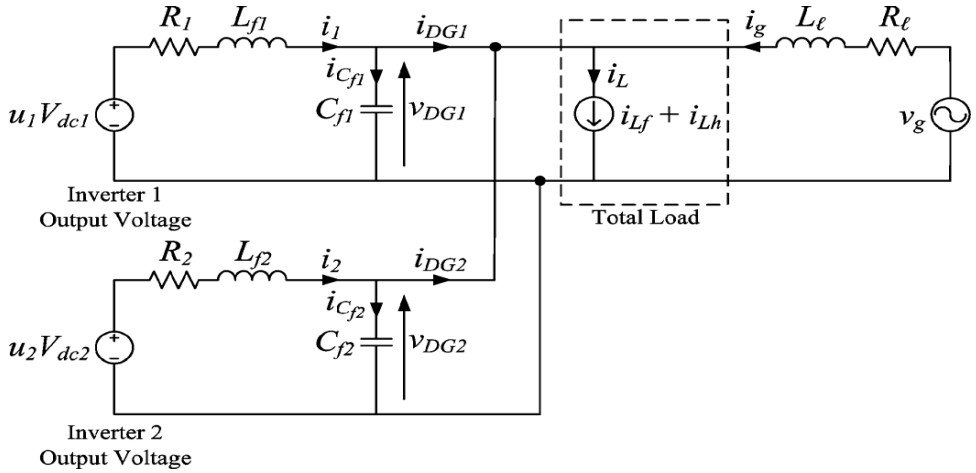

Fig. 5. Equivalent single-phase representation of the DG for islanded operation.

B. DG Inverter Modeling

Figs. 4 and 5 show the equivalent single-phase representation of the DG inverters for grid-connected and islanded operation, respectively [13]–[15]. The switched voltage across the output of the th DG inverter is represented by $u_i V_{dcj}$ where u_i is the control input and $j = 1,2$ The output of the DG inverter is interfaced with an LC filter represented by L_{fi} and C_{fi} to eliminate the high switching frequency harmonics generated by the DG inverter. The resistance R_i models the loss of the DG inverter. The total load current i_L , which is the sum of the currents delivered to the load k, is given by

$$\boldsymbol{i_L = \sum_{k=1,2,3} i_{LK} = i_{L1} + i_{L2} + i_{L3}} \quad \textbf{(4)}$$

and can be modeled as two components consisting of fundamentals i_{Lf} and harmonic i_{Lh} with their peak amplitudes I_{Lf} and I_{Lh} respectively, and is represented by

$$\boldsymbol{i_L = i_{Lf} + i_{Lh} = I_{Lf} \sin(\omega t - \varphi_{Lf}) + \sum_{h=3,5,\ldots}^{N} I_{Lh} \sin(h\omega t - \varphi_{Lh})}$$

$$= I_{Lf} \sin \omega t \cos \varphi_{Lf} - I_{Lf} \cos \omega t \sin \varphi_{Lf}$$
$$+ \sum_{h=3,5\ldots}^{N} I_{Lh} \sin(h\omega t - \varphi_{Lh})$$
$$= i_{Lf,p} + i_{Lf,q} + i_{Lh} \quad (5)$$

where φ_{Lf} and φ_{Lh} are the respective phase angles of the fundamental and harmonic components of i_L, and $i_{Lf,p}$ and $i_{Lf,q}$ are the instantaneous fundamental phase and quadrature components of i_L. To achieve unity power factor at the grid side, compensate for the harmonics in the load currents and concurrently achieve load sharing, the inverter of the DG unit supplies a current i_{DGj} that is given by

$$i_{DGj} = (i_{Lf,p} - i_g) + i_{Lf,q} + i_{Lh} \quad (6)$$

where i_g is the grid current. As shown in Fig. 4, the distribution grid is supplied by a utility substation represented by a voltage source u_g during grid-connected operation, and is connected to the microgrid and the loads via a distribution line with resistance R_l and inductance L_l. In the grid-connected mode, the grid voltage is known and the microgrid shares the load demand with the grid. Hence, to

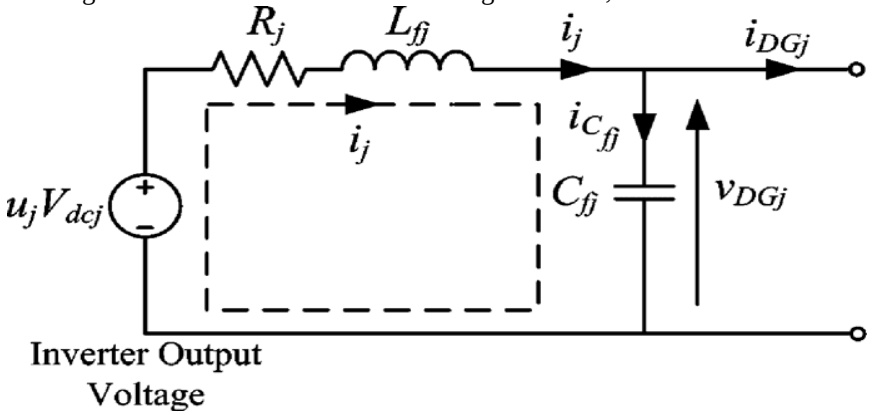

Fig. 6. Single-phase representation of the the DG inverter for grid-connected and islanded operations

Control the power delivered to the loads, the output current of the DG inverter is controlled using the current control mode (CCM). During islanded operation, the microgrid will supply the overall load demand as shown in Fig. 5, and it is required that the output voltage be regulated to a pure sine wave with a fixed magnitude. This can be achieved through the voltage-control mode (VCM). The control design for the DG inverter will be elaborated on further in Section III. To derive a state-space model for the DG inverter during both grid-connected and islanded operations, Kirchhoff's voltage and current laws are applied to the current loop i_j as shown in Fig. 6, and the following equations are obtained:

$$\frac{di_j}{dt} = -\frac{R_j}{L_{fj}} i_j - \frac{1}{L_{fj}} u_{DGj} + \frac{V_{dcj}}{L_{fj}} u_j \quad (7)$$

$$\frac{du_{jDGj}}{dt} = -\frac{1}{C_{fj}} i_j + \frac{1}{C_{fj}} i_{DGj} \quad (8)$$

where i_j is the current passing through L_{fj}. Hence, the gridconnected DG inverter model can be written as

$$\dot{x_{gj}} = A_{gj} x_{gj} + B_{gj1} u'_j + B_{gj2} u_j \quad (9)$$

$$y_{gj} = C_{gj} x_{gj} + D_{gj1} u'_j + D_{gj2} u_j \quad (10)$$

where the subscripts g and j represent the model of DG inverter j during grid-connected operation and

$$A_{gj} = -\frac{R_j}{L_{fj}}\ ;\ B_{gj1} = [-\frac{1}{L_{fj}} \quad 0]\ ;\ B_{gj2} = \frac{V_{dcj}}{L_{fi}}\ ;\ C_{gj} = 1$$
$$D_{j1} = [0 \quad -C_{fj}];\ D_{gj2} = 0$$

$x_{gj} = i_j$ is the state; $u'_j = [u_{DGj} \quad du_{dgj}/dt]^T$ exogenous input; u_j is the control input, with $-1 \leq u_j \leq 1$; and $y_{gj} = i_{DGj}$ is the output, which will be regulated to track the desired periodic reference waveform. During islanded operation, the frequency will change due to power imbalance in the microgrid. This change in frequency is detected by the EMS of the microgrid, which is used to manage and monitor the power dispatch by each DG unit. Based on the frequency change information, the EMS will require the main DG unit and the SB to generate the necessary power to meet the overall load demand in the microgrid as shown in the flowchart of Fig. 3, such that (1) is satisfied. During islanded operation, it follows from (7) and (8) that DG inverter can be modeled as

$$\dot{x_{ij}} = A_{ij} x_{ij} + B_{ij1} i'_j + B_{ij2} u_j \quad (11)$$
$$y_{ij} = C_{ij} x_{ij} + D_{ij1} i'_j + D_{ij2} u_j \quad (12)$$

where the subscript i denotes the model of the DG inverter j during islanded operation(j =1,2) and

$$A_{ij} = \begin{bmatrix} -\frac{R_j}{L_{fj}} & -\frac{1}{L_{fj}} \\ \frac{1}{C'_f} & 0 \end{bmatrix}; B_{ij1} = \begin{bmatrix} 0 \\ -\frac{1}{C'_f} \end{bmatrix}; B_{ij2} = \begin{bmatrix} \frac{V_{dcj}}{L_{fj}} \\ 0 \end{bmatrix}$$
$$C_{ij} = \begin{bmatrix} 0 & 1 \\ 1 - \frac{C_{fj}}{C'_f} & 0 \end{bmatrix}; D_{ij1} = \begin{bmatrix} 0 \\ \frac{C_{fj}}{C'_f} \end{bmatrix}; D_{ij2} = \begin{bmatrix} 0 \\ 0 \end{bmatrix}$$

With $C'_f = \sum_{j=1}^{2} C_{fj}$; $x_{ij} = [i_j \quad u_{DGj}]^T$ is the state vector; $i'_j = i_L - \sum_{n \neq j} i_n$ is the exogenous input of the DG inverter j; u_j is the control input, with -1≤ u_j ≤1 and $y_{ij} = [u_{DGj} \quad i_{DGj}]^T$ is the output, which will be regulated to track the desired reference waveform. Note that although the emphasis is on the voltage u_{DGj}, both u_{DGj} *and* i_{DGj} will be regulated in the VCM to ensure that the power is delivered. Furthermore, it is assumed that the exogenous input i'_j in the model is not directly measurable by the DG inverter j since it involves quantities outside that inverter. Precisely, i'_j represents the sum of all load currents i_L minus the sum of all i_n from the other DG inverters $n \neq j$ in the microgrid. Although only one other inverter has been presented in the proposed microgrid, the model is extendable to more DG inverters.

III. Control Design

With the mathematical model presented in Section II-B, this paper proposes a novel MPC algorithm for the control of the DG inverters of the microgrid. The proposed algorithm is a newly developed MPC algorithm specifically designed for fast-sampling systems, to track periodic signals so as to deal with the dual-mode operation of the microgrid. The algorithm decomposes the MPC optimization into a steady-state sub-problem and a transient sub-problem, which can be solved in parallel in a receding horizon fashion. Furthermore, the steady-state sub problem adopts a dynamic policy approach in which the computational complexity is adjustable. The decomposition also allows the steady-state sub-problem to be solved at a lower rate than the transient sub-problem if necessary. These features help to achieve a lower computational complexity and make it suitable for implementation in a fast-sampling system like our microgrid applications. In the simulation studies in this paper, the sampling interval is chosen as 0.2ms, which is considered pretty small in conventional MPC applications, but necessary for the high order of harmonics being tackled for our problem. According to [16], sampling in the range of tens of kHz is possible with state-of-the-art code generation techniques. It is noted that in either the grid-connected or the islanded operation, the state-space model of Section II-B after time-discretization will take the form

$$\boldsymbol{x}^+ = \boldsymbol{Ax} + \boldsymbol{B_1 w} + \boldsymbol{B_2 u} \quad (13)$$
$$\boldsymbol{y} = \boldsymbol{Cx} + \boldsymbol{D_1 w} + \boldsymbol{D_2 u} \quad (14)$$

where the superscript + represents the time-shift operator (with sampling interval T_s), and the exogenous signal ω is periodic. In general, any periodic signal with a finite number of harmonics can be written as the output of an autonomous finite-dimensional linear time-invariant state-space model. Furthermore, the initial state of this autonomous model determines the magnitude and phase angle of this periodic signal. Hence, the exogenous signal in (13) and (14) together with the reference that in (14) desires to track can be modeled by

$$\boldsymbol{\varepsilon}^+ = \boldsymbol{A_\epsilon \varepsilon} \quad (15)$$
$$\boldsymbol{\omega} = \boldsymbol{C_\omega \varepsilon}$$
$$\boldsymbol{d} = \boldsymbol{C_d \varepsilon} \quad (17)$$

for some A_ϵ , C_ω and C_d as described above. For the CCM during grid-connected operation, $y = i_{DG}$ and the current reference for i_{DG} to track consist of the same order of harmonics as i_L and is derived from the desired active and reactive power outputs of the DG units generated by the EMS. On the other hand, for the VCM as described in Section II-B during islanded operation, $y = [u_{DG} \quad i_{DG}]^T$ for the DG unit and the reference $d = [du_{DG} \quad di_{DG}]$ consists of a voltage reference and a current reference. The voltage reference du_{DG} for u_{DG} to track is typically a pure sine wave, which is derived from the monitored prior to islanding. To ensure that the respective DG units deliver the necessary power for stable operation of the microgrid during islanded operation, the current reference i_{DG} for di_{DG} to track is regulated according to the power reference generated by the EMS.
The state-space model given by (15)–(17) is known as the exogenous system in this paper. Although only odd harmonics up to the 29th order have been considered, the methodology can be easily extended to include even harmonics. The exogenous state ϵ, which essentially represents the sets of Fourier coefficients of ω and d , can be automatically identified using a Kalman-based observer known as the exogenous Kalman filter once the signal ω is measured and the reference d is specified. The exogenous Kalman filter is given by

$$\tilde{\xi}^{+} = A_{\xi}\tilde{\xi} + L_w(w - \tilde{w}) + L_d(d - \tilde{d}) \quad (18)$$

$$\tilde{w} = C_w\tilde{\xi} \quad (19)$$

$$\tilde{d} = C_d\tilde{\xi} \quad (20)$$

where is the estimated exogenous state L_w, and L_d are the observer gain matrices of the Kalman filter, and the terms $(\omega - \tilde{\omega})$ and $(d - \tilde{d})$ are essentially the difference between the actual ω, d and the estimated $\tilde{\omega}, \tilde{d}$ generated from the Kalman filter, such that $(\omega - \tilde{\omega})$ and $(d - \tilde{d})$ should tend to zero asymptotically. Since is actually a Fourier decomposition of the periodic signals ω and d , the exogenous Kalman filter given by (18)–(20) functions like a harmonic extraction circuit from the power system point of view [17], [18]. In what follows, the control u in (13) and (14) is decomposed into a steady-state control u_s and a transient control u_t as

$$u = u_s + u_t \quad (21)$$

such that $u \to u_s$ and $u \to u_t$ asymptotically. Both u_s and u_t will employ aMPC strategy, but the formerwill adopt a dynamic MPC policy whereas the latter will adopt a more conventional finite-horizon approach.

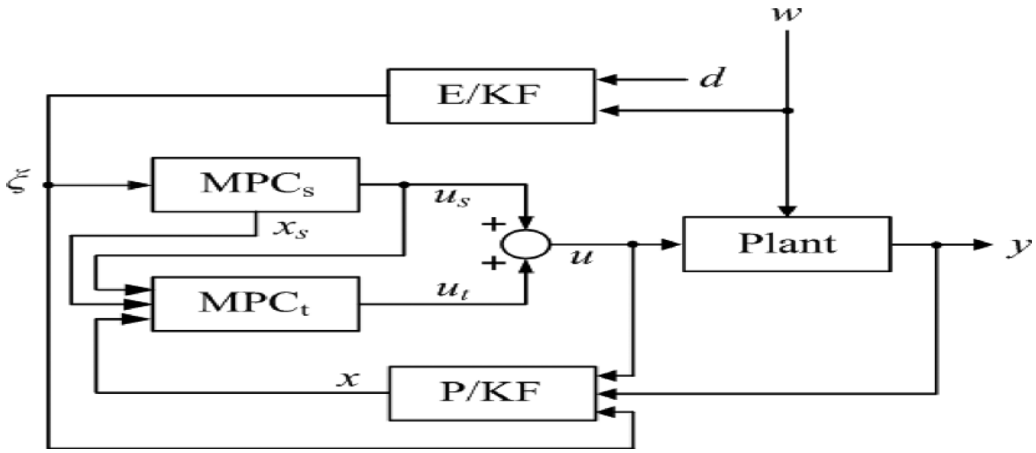

Fig. 7. Overall MPC controller for the DG inverter with E/KF denoting the exogenous Kalman filter and P/KF denoting the plant Kalman filter

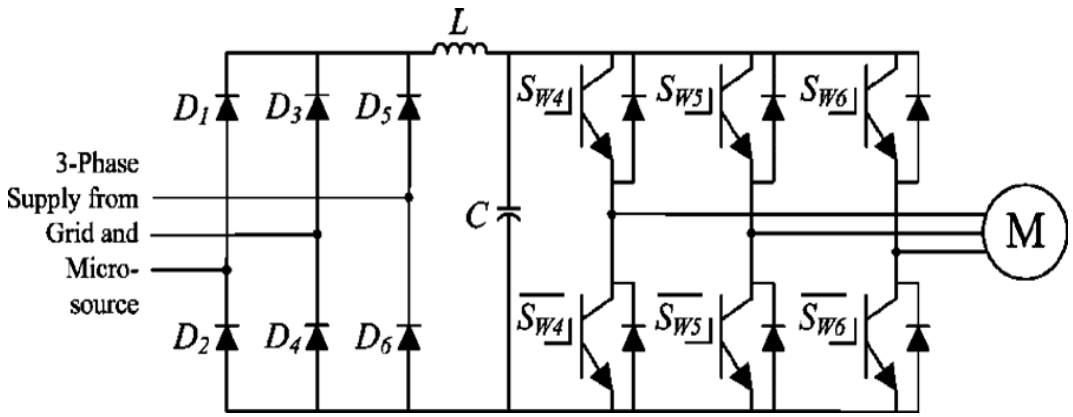

Fig. 8. Configuration of a 15-kVA three-phase ASD.. and (14). Similar to the case of the exogenous Kalman filter, the plant Kalman filter is given by

$$\tilde{\boldsymbol{x}} = \boldsymbol{A}\tilde{\boldsymbol{x}} + \boldsymbol{B_1 w} + \boldsymbol{B_2 u} + \boldsymbol{L_y}(\boldsymbol{y} - \tilde{\boldsymbol{y}})$$

$$\tilde{\boldsymbol{y}} = \boldsymbol{c}\tilde{\boldsymbol{x}} + \boldsymbol{B_1 w} + \boldsymbol{B_2 u}$$

where$\tilde{x}$ is the estimated plant L_y state and is the observer gain matrix of the plant Kalman filter, and the term $(\boldsymbol{y} - \tilde{\boldsymbol{y}})$ is the difference between the actual measured output and the estimated output . The overall configuration of the proposed control algorithm combining the steady-state control and the transient control is shown in Fig. 7.

IV. Simulation Studies

The simulation model of the microgrid shown in Fig. 1 is realized in Matlab/Simulink. The microgrid is tested under various conditions to evaluate its capabilities when operating connected and islanded from the distribution grid. Three different load types consisting of linear and nonlinear loads are considered in the studies. For load 1, a 15-kVA three-phase PWM adjustable speed drive (ASD) with its configuration as shown in Fig. 8 is used and load 2 is made up of a three-phase RL load rated at P_{L2}= 28 kW and Q_{L2}= 18.5 kVAr. Load 3 is a noncritical three-phase dimmer load rated at P_{L3}=18 kW and Q_{L3}= 12.3 kVAr, which is nonlinear in nature and will be shed under emergency conditions when the generation of the microgrid is unable to meet the load demand. The per-phase currents , i_{L1}, i_{L2} and i_{L3}drawn by loads 1, 2, and 3 for $0 \leq t < 0.2s$ are shown in Fig. 9. The system parameters are given in Table I. The impedances of the DG inverters and distribution line have been coarsely estimated since these values are not precisely known in practice.

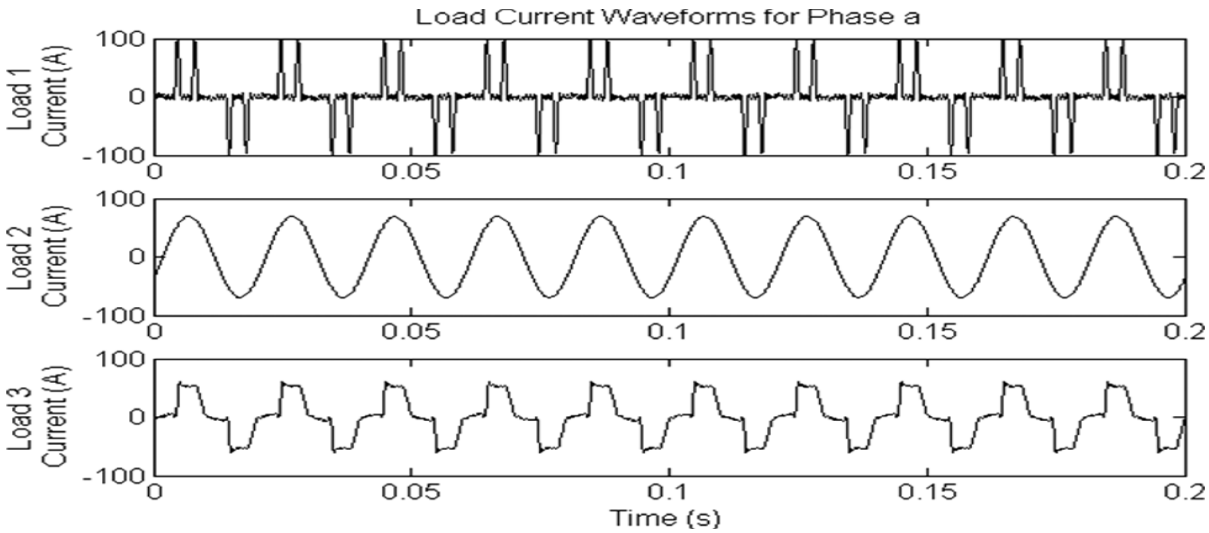

Fig. 9. Per-phase currents drawn by loads 1, 2, and 3.

TABLE
PARAMETERS OF THE PROPOSED SYSTEM

Parameter	Value
Distribution grid voltage	v_g =230V (phase)
DC link voltage	V_{dc} =400V
Distribution line impedance	$R_\ell = 0.0075\Omega$, $L_\ell = 25.7\mu H$
LC filter	L_f= 1.2mH, C_f= 20μF
DG inverter loss resistance	R_f=0.01 Ω

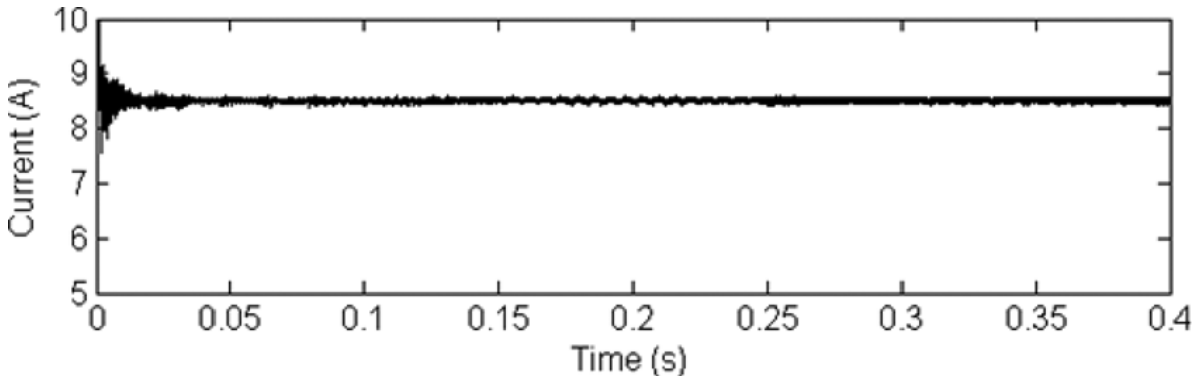

Fig. 10. Waveform of the SB current during charging

A. Test Case 1: *Power Quality Improvement With Load-Sharing During Grid-Connected Operation*

The first test case demonstrates the capability of the microgrid to improve the power quality of the distribution network by compensating for the harmonics in the total load current due to the nonlinear loads that are connected to the distribution network, such that the harmonics will not propagate to the rest of the distribution network during grid-connected operation. In this test case, the main DG unit accounts for 20% of the total load demand. The SB is operating in the charging mode to store energy during off-peak period where the cost of generation from the grid is low to meet future sudden demands for power. The SB current (as shown in Fig. 1) and the SOC during charging for $0 \leq t < 0.4$ s are shown in Figs. 10 and 11, respectively. The waveforms of the total load current , the current supplied by the main DG unit and grid current under this test case are shown in Fig. 12. The unsteady measurements in and as shown in Fig. 12(middle) and Fig. 12(bottom) respectively during initialization for $0 \leq t < 0.06s$ are due to the factthat the controller needs a period of 3 cycles to track the generated references. During steady-state condition, the total harmonic distortion (THD) value of i_L is 42.1% as shown in Fig. 12 (top). With the main DG unit compensating for the harmonic currents as shown in Fig. 12 (middle), the THD value of i_g is improved to about 0.4% as shown in Fig. 12 (bottom). To achieve power factor correction at the grid side, the main DG unit is also controlled to provide the reactive component $i_{Lf,q}$ of the current i_L as given in (5). Fig. 13 shows closed-up waveforms of the grid voltage v_g and i_g of phase a for $0.2 \leq t < 0.24s$. It is observed that the waveform of i_g is in phase with v_g that of with power factor correction.

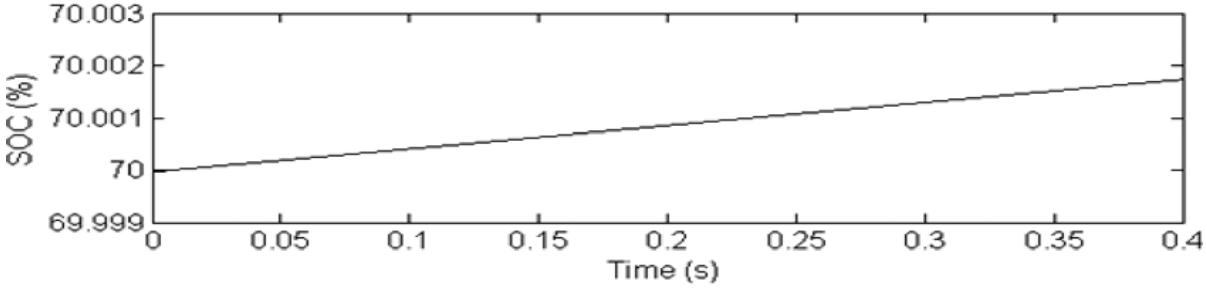

Fig. 11. SOC of the SB during charging

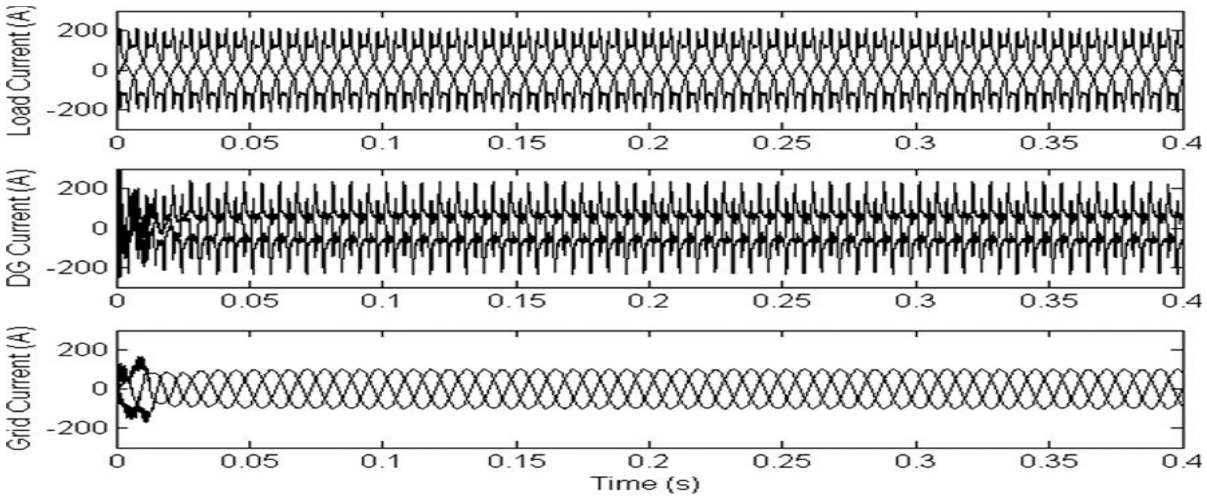

Fig. 12. Waveforms of three-phase load current (top), three-phase DG current (middle), and three-phase grid current (bottom)

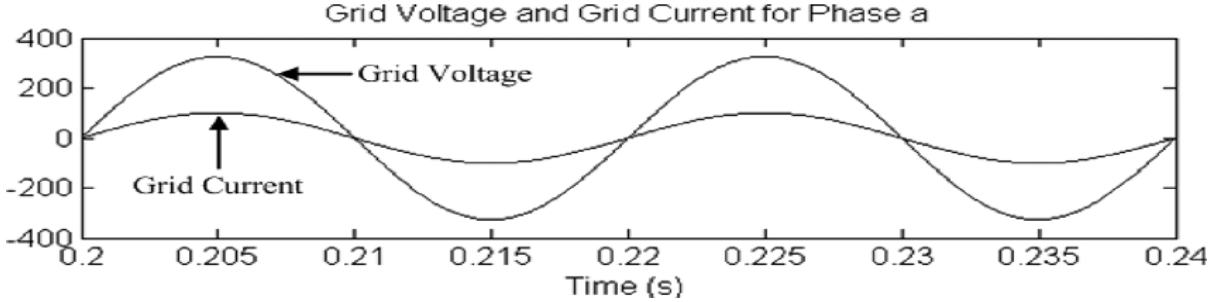

Fig. 13. Waveforms of grid voltage and grid current for phase a

The total real and reactive power delivered to the loads is about 58 kW and 35 kVAr as shown in the power waveforms of Fig. 14. The real power dispatched by the main DG unit is 11.6 kW (20% of the real power consumed by the loads) as shown in Fig. 15, which demonstrates the capability of the main DG unit to dispatch the required power. The main DG unit also delivers all of the reactive power required by the loads to achieve unity power factor at the grid side. The real and reactive power delivered by the grid is shown in Fig. 16. It can be observed from Fig. 16 that the grid supplies 80% (46.4 kW) of the total real power delivered to the loads and dispatches an additional power of about 3 kW to charge the SB. It is also observed that the reactive power supplied by the grid is zero, resulting in unity power factor at the grid side.

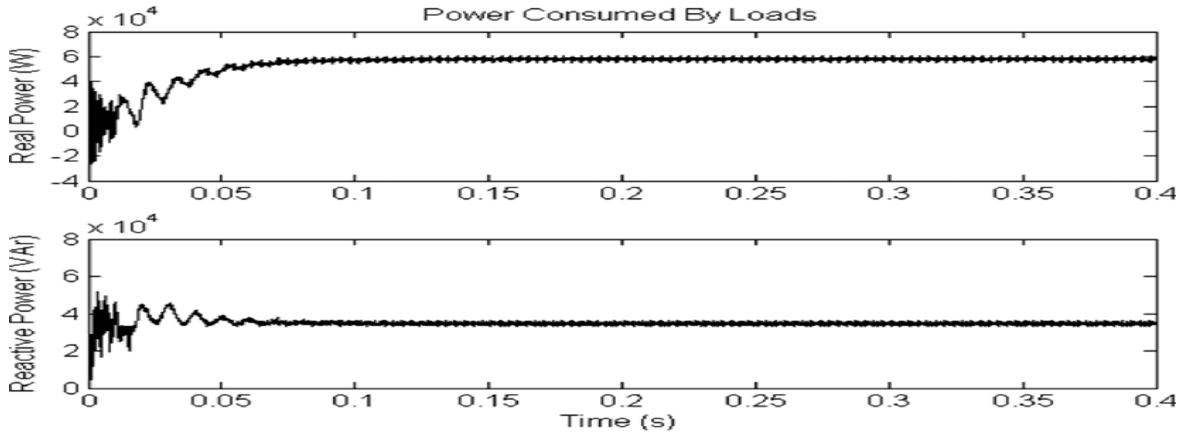

Fig. 14. Real (top) and reactive (bottom) power consumed by loads

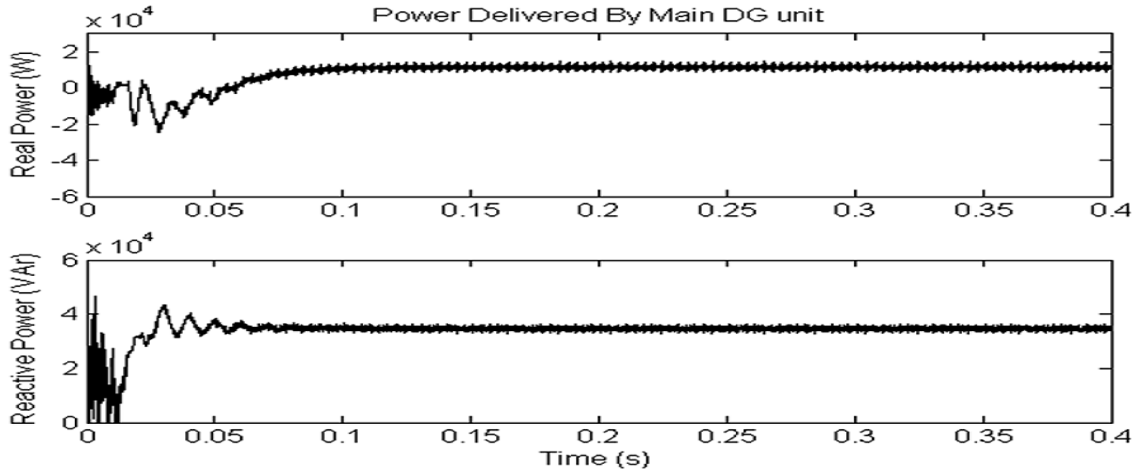

Fig. 15. Real (top) and reactive (bottom) power delivered by the main DG unit

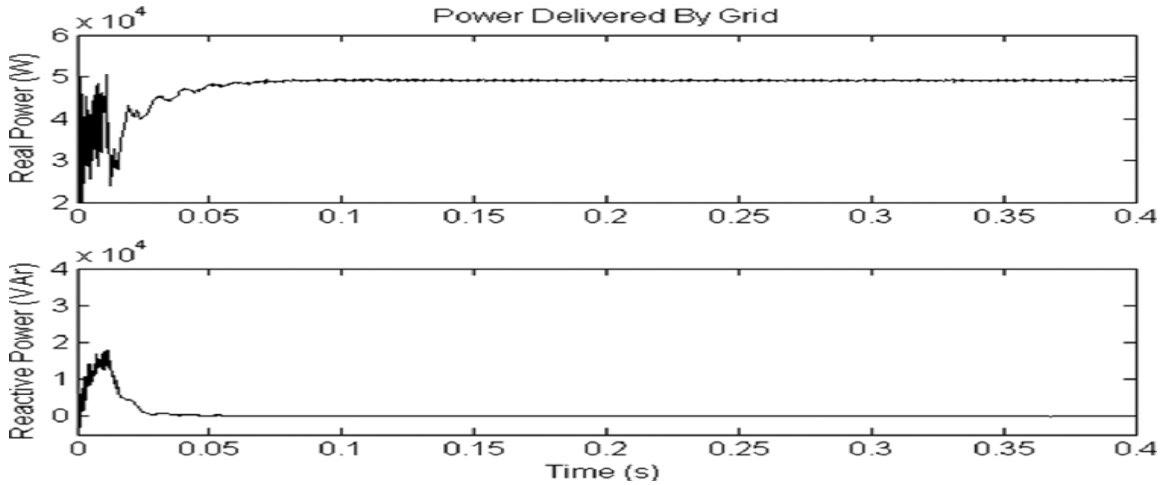

Fig. 16. Real (top) and reactive (bottom) power delivered by the grid

B. Test Case 2: *Peak Shaving of Loads During Peak Periods*

The electricity pricing in many countries is impacted by the TOU tariffs. In DSM, energy-storage devices can be used to reduce the burden of generation of power directly from the distribution grid during peak periods. The second test case demonstrates the operation of the microgrid to achieve peak shaving in order to reduce the cost of generation from the grid when consumers practice DSM. Fig. 17 shows a typical hourly demand response curve in a day indicated by the solid line. As in test case 1, the main DG unit is controlled to deliver 20% of the load demand. To achieve peak shaving at 11:00 h, the SB is operating in the discharge mode to provide 20% (11.6 kW) of the load demand. With a further reduction of 20% in the power supplied by the grid, the total load demand at 11:00 h is reduced by a total of 40% as shown by the dotted line in Fig. 17. The power waveforms of the grid for $o \leq t <$ 0.4 s are shown in Fig. 18. It can be seen from Fig. 18 that the real power deliveredby the grid is 60% (34.8 kW) of the load demand with peak shaving, and the reactive power supplied is zero with the main DG unit compensating for the reactive components of the load currents. The real power waveform delivered by DG inverter 2 (as shown in Fig. 1) of the SB during discharging is shown in Fig. 19. It can be observed from Fig. 19 that the SB delivers the required real power of about 20% (11.6 kW) of the load demand during peak shaving.

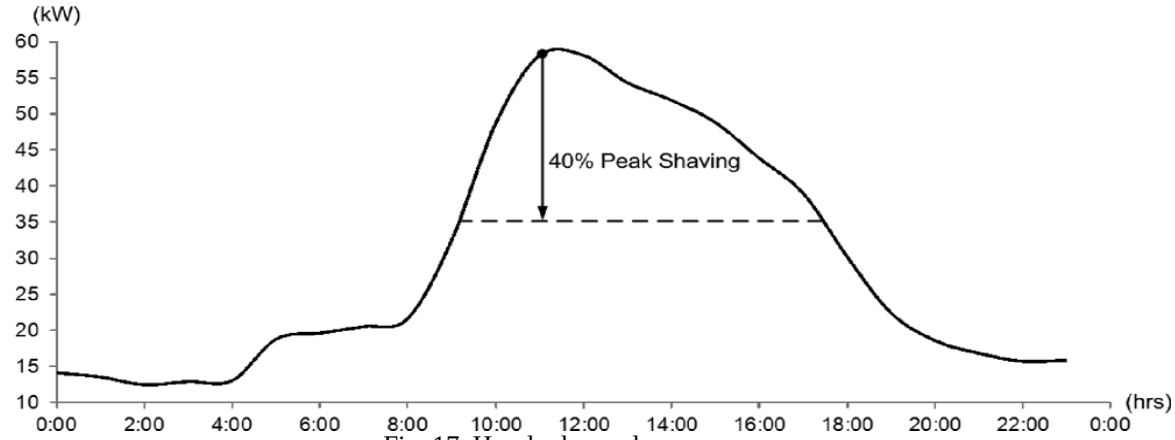

Fig. 17. Hourly demand response curve

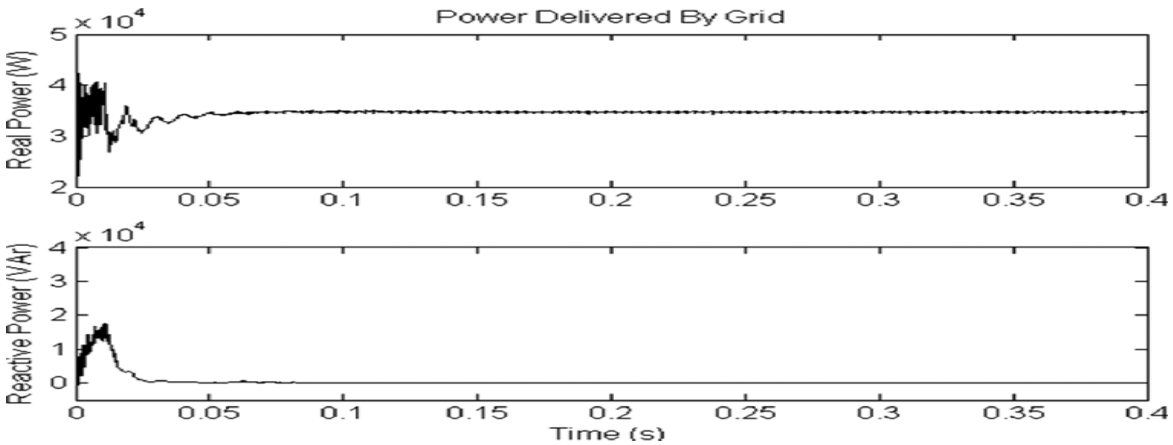

Fig. 18. Real (top) and reactive (bottom) power delivered by the grid

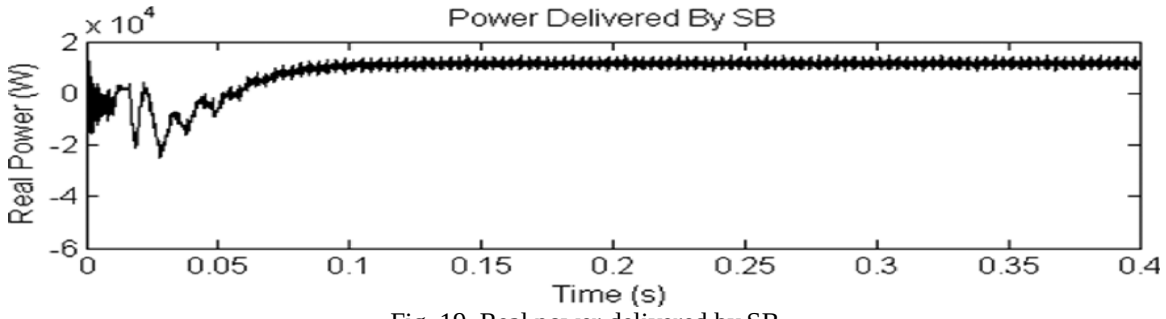

Fig. 19. Real power delivered by SB

C. Test Case 3: *Load Shedding During Islanded Operation*

During islanded operation, the total generation of the microgridmight not be able to sustain its generation tomeet the power demand of the loads. Under such circumstances, consumers participating in DRM will allow the non-critical load to be shed so as to maintain the stable operation of the microgrid. The third test case demonstrates the operation of the microgrid when it islands from the grid. In this test case, the microgrid is initially operating in the grid-connected mode for $o \leq t < 0.2$ s. The SB is initially operating in the idle mode and its SOC is 80%. A fault occurs on the upstream network of the distribution grid and the CB operates to disconnect the microgrid from the distribution grid at t=0.2 s.Fig. 20 shows the waveforms of the real and reactive power supplied by the grid. It can be seen from Fig. 20 that the CBmanages to fully isolate the microgrid from the distribution grid in about half a cycle, resulting in zero real and reactive power delivered by the grid for $0.2 \leq t < 0.6$ s. The real power delivered by DG inverter 2 of the SB is shown in Fig. 21. For $0 \leq t < 0.2$ s, the SB is in the idle mode. After the initiation of the islanding operation at t= 0.2 s, theDGinverter 2 is tasked by theEMS to increase its generation to provide real power of about 12.5 kW to the loads which reach steady-state operation in about 3 cycles. With only the main DG unit and the SB supplying for the loads, the power imbalance results in a decrease in the system frequency, which is detected by the EMS. To maintain the stability of the microgrid during islanded operation, the shedding of load 3 ($P_{L3=}$18 kW and Q_{L3}= 12.3 kVAr) is also initiated at t= 0.4 s by the EMS such that the total generation from the main DG unit (P_{DG}=27.5 kWand Q_{DG} =22.7 kVAr) and the SB (P_b=12.5 kW) can meet the power demand by the loads. A delay of $0 \leq t < 0.2$ s is introduced between islanding of the microgrid and load shedding to cater for frequency transients that might occur momentarily due to the energization of large motor loads. The waveforms of the real and reactive power delivered to the loads for 0 0.6 s are shown in Fig. 22. It can be observed from Fig. 22 that when load 3 is shed at t=0.4s, the total real and reactive power delivered to the loads gradually decreases to settle and operate stably at about 40 kW and 22.7 kVAr, respectively, in about 3 cycles.

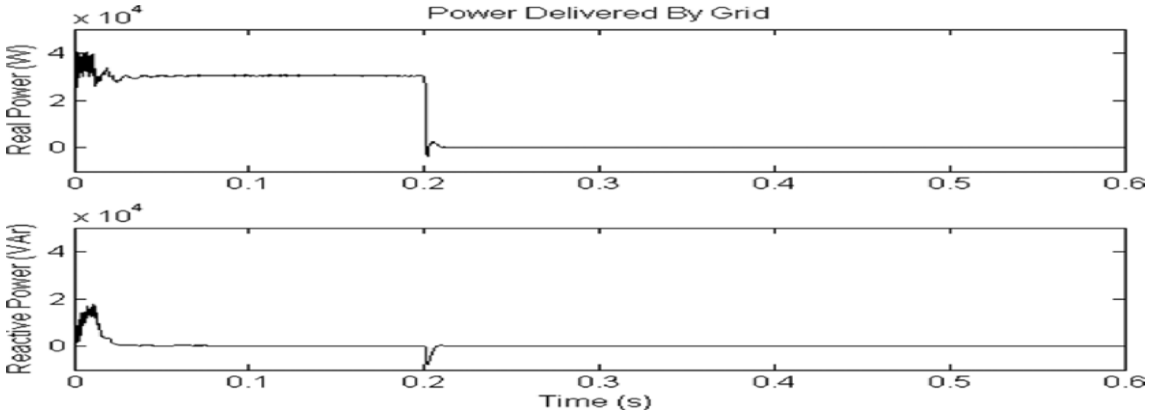

Fig. 20. Real (top) and reactive (bottom) power delivered by the grid

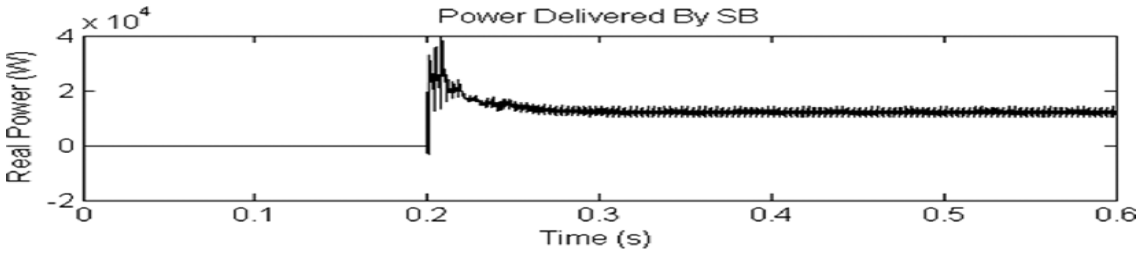

Fig. 21. Real power delivered by SB.

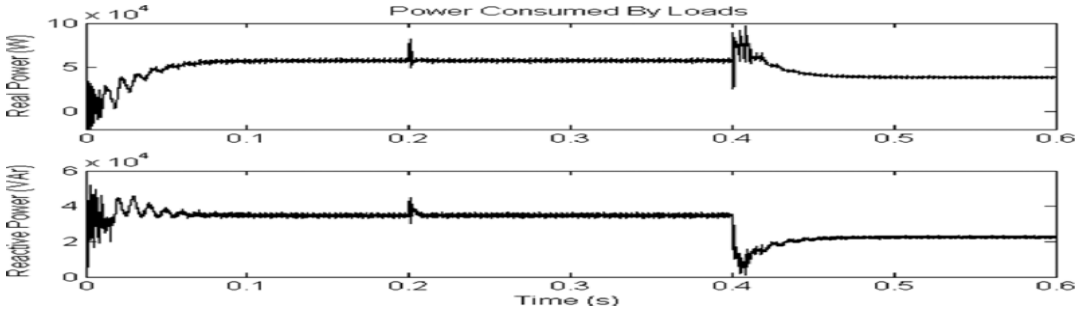

Fig. 22. Real (top) and reactive (bottom) power consumed by loads

V. Conclusion

In this paper, a control system that coordinates the operation of multiple DG inverters in a microgrid for grid connected and islanded operations has been presented. The proposed controller for the DG inverters is based on a newly developed MPC algorithm which decomposes the control problem into steady-state and transient subproblems in order to reduce the overall computation time. The controller also integrates Kalman filters into the control design to extract the harmonic spectra of the load currents and to generate the necessary references for the controller. The DG inverters can compensate for load harmonic currents in a similar way as conventional compensators, such as active and passive filters, and, hence, no additional equipment is required for power-quality improvement. To realize the smart grid concept, various energy-management functions, such as peak shaving and load shedding, have also been demonstrated in the simulation studies. The results have validated that the microgrid is able to handle different operating conditions effectively during grid-connected and islanded operations, thus increasing the overall reliability and stability of the microgrid.

REFERENCES

[1] S. Braithwait, "Behaviormanagement," IEEE Power and EnergyMag., vol. 8, no. 3, pp. 36–45, May/Jun. 2010.
[2] N. Jenkins, J. Ekanayake, and G. Strbac, Distributed Generation. London, U.K.: IET, 2009.
[3] M. Y. Zhai, "Transmission characteristics of low-voltage distribution networks in China under the smart grids environment," IEEE Trans. Power Del., vol. 26, no. 1, pp. 173–180, Jan. 2011.
[4] G. C. Heffner, C. A. Goldman, and M. M. Moezzi, "Innovative approaches to verifying demand response of water heater load control," IEEE Trans. Power Del., vol. 21, no. 1, pp. 1538–1551, Jan. 2006.
[5] R. Lasseter, J. Eto, B. Schenkman, J. Stevens, H. Vollkommer, D. Klapp, E. Linton, H. Hurtado, and J. Roy, "Certs microgrid laboratory test bed, and smart loads," IEEE Trans. Power Del., vol. 26, no. 1, pp. 325–332, Jan. 2011.
[6] A. Molderink, V. Bakker, M. G. C. Bosman, J. L. Hurink, and G. J. M. Smit, "Management and control of domestic smart grid technology," IEEE Trans. Smart Grid, vol. 1, no. 2, pp. 109–119, Sep. 2010.
[7] A. Mohsenian-Rad, V. W. S.Wong, J. Jatskevich, R. Schober, and A. Leon-Garcia, "Autonomous demand-side management based on gametheoretic energy consumption scheduling for the future smart grid," IEEE Trans. Smart Grid, vol. 1, no. 3, pp. 320–331, Dec. 2010.
[8] S. Chowdhury, S. P. Chowdhury, and P. Crossley, Microgrids and Active Distribution Networks. London, U.K.: IET, 2009.
[9] A. Yazdani and P. P. Dash, "A control methodology and characterization of dynamics for a photovoltaic (PV) system interfaced with a distribution network," IEEE Trans. Power Del., vol. 24, no. 3, pp. 1538–1551, Jul. 2009.
[10] K. T. Tan, P. L. So, Y. C. Chu, and K. H. Kwan, "Modeling, control and simulation of a photovoltaic power system for grid-connected and stand-alone applications," in Proc. Int. Power Energy Conf., 2010, vol. 56, pp. 608–613.
[11] M. Charkhgard and M. Farrokhi, "State-of-charge estimation for lithium-ion batteries using neural networks and EKF," IEEE Trans. Ind. Electron., vol. 57, no. 12, pp. 4178–4187, Jun. 2010.
[12] M. Coleman, C. K. Lee, C. Zhu, and W. G. Hurley, "State-of-charge determination from EMF voltage estimation: Using impedance, terminal voltage, and current for lead-acid and lithium-ion batteries," IEEE Trans. Ind. Electron., vol. 54, no. 5, pp. 2550–2557, Oct. 2007.
[13] A. Gosh and G. Ledwich, Power Quality Enhancement Using Custom Power Devices. Norwell, MA: Kluwer, 2002, pp. 380–406.
[14] J.M.Guerrero, J. Matas, L. Garcíade Vicuña, M. Castilla, and J.Miret, "Decentralized control for parallel operation of distributed generation inverters using resistive output impedance," IEEE Trans. Ind. Electron., vol. 54, no. 2, pp. 994–1004, Apr. 2007.
[15] C. L. Chen, Y. B.Wang, J. S. Lai,Y. S. Lai, and D. Martin, "Design of parallel inverters for smooth mode transfer of microgrid applications," IEEE Trans. Ind. Electron., vol. 25, no. 1, pp. 6–15, Jan. 2010.
[16] J. Mattingley, Y. Wang, and S. Boyd, "Receding horizon control: Automatic generation of high-speed solvers," IEEE Control Syst. Mag., vol. 31, no. 3, pp. 52–65, Jun. 2011.
[17] J. A. Macias and A. Gomez, "Self-tuning of Kalman filters for harmonic computation," IEEE Trans. Power Del., vol. 21, no. 1, pp. 501–503, Jan. 2006.
[18] V. Moreno, A. Pigazo, and R. I. Diego, "Reference estimation technique for active power filters using a digital Kalman algorithms,"